ACS OMEGA

Open Access

This article is licensed under CC-BY-NC-ND 4.0

http://pubs.acs.org/journal/acsodf

Article

3D Extrusion-Printed Alginate–Gelatin Hydrogel Modified with Nanoscale Hydroxyapatite: A Comprehensive Understanding of Process Science and Evaluation of the Antimicrobial Property

Sulob Roy Chowdhury, Krittika Dey, and Bikramjit Basu*

Cite This: *ACS Omega* 2025, 10, 18428–18443

Read Online

ACCESS | Metrics & More | Article Recommendations

ABSTRACT: In developing hydrogel scaffolds for the soft tissue regeneration, a number of inorganic or carbonaceous fillers are embedded in alginate/gelatin-based hydrogel while manufacturing shape fidelity compliant constructs using three-dimensional (3D) extrusion printing. Among the spectrum of nanofillers, nanohydroxyapatite (nHAP), due to its intrinsic bioactivity, could promote mineralization and interaction with host tissues while conferring superior mechanical properties (strength and elastic modulus). Against this backdrop, this study demonstrates the effectiveness of nHAP reinforcement in tuning several clinically relevant properties such as rheological properties, mechanical properties, swelling, degradation, and antimicrobial properties. At higher concentrations of nHAP (0.75%) in the hydrogel matrix (3A5G0.75H), a 3.13-fold increment in the compressive strength was observed, with the gel stability window and the thermal stability of the cross-linked graft being extended to greater than 40 and 143 °C, respectively. This study demonstrated the printability of the nHAP-reinforced hydrogel ink by fabricating the matrix-shaped graft of dimension 20 mm in diameter and 10 mm in thickness, and the buildability was established by making the bulk-sized construct up to 62 layers (20 mm in height) with a well-maintained pore interconnectivity, as demonstrated using micro-CT analysis. Interestingly, the CFU study revealed a 2.9- and 1.5-fold improvement in the reduction of bacterial adhesion for 3A5G0.75H with respect to *Escherichia coli* and *Staphylococcus aureus* bacteria. Cell culture studies on the 3D printed scaffolds w.r.to NIH 3T3 fibroblast cell line demonstrated a consistent increase in cell viability and pronounced filopodial extensions, confirming the cytocompatibility of 3A5G0.75H scaffolds and their ability to support cellular growth during an *in vitro* culture. Taken together, the present study uncovers a process science-based understanding of the 3D buildability and biophysical properties of different concentrations of nHAP-reinforced hydrogel inks with clinically relevant properties.

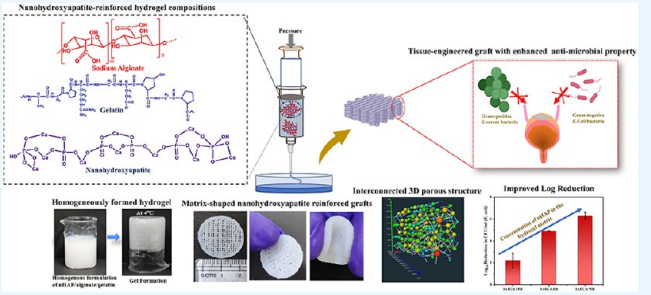

1. INTRODUCTION

Tissue engineering and organ transplantation are integral to contemporary regenerative medicine, addressing the escalating demand for viable solutions in tissue repair and organ replacement.[1,2] Tissue engineering employs a combination of biomaterials, cellular components, and bioactive molecules to fabricate functional tissue constructs, providing potential alternatives to traditional organ transplantation approaches.[3−5] While organ transplantation is a life-saving procedure, it is confronted with challenges such as a shortage of donor organs, immune rejection, and ethical considerations.[6−8] By advancing biomaterials, cellular technologies, and bioengineering methodologies, tissue engineering seeks to create bioengineered tissues and organs, thereby mitigating dependence on donor organs and addressing issues related to immunosuppression and transplantation ethics.[9−12]

Among biopolymer-based hydrogels, alginate–gelatin scaffolds stand out for their significant advancements in complex soft tissue engineering. Alginate, a linear polysaccharide derived from brown algae, is composed of repeating β-D-mannuronic acid and α-L-guluronic acid units. These units form a highly hydrated, three-dimensional (3D) network through ionic cross-linking with divalent cations like Ca^{2+}, resulting in scaffolds with tunable mechanical properties and controlled degradation rates.[13,14] This flexibility is crucial for developing scaffolds that can accommodate the unique mechanical and biological demands of soft tissues.[15,16]

Gelatin, derived from the partial hydrolysis of collagen, retains repeating glycine–proline–X sequences, where X varies

Received: November 26, 2024
Revised: February 19, 2025
Accepted: April 14, 2025
Published: May 2, 2025

© 2025 The Authors. Published by American Chemical Society

among amino acids. Although gelatin's triple-helix structure is partially disrupted, it still provides essential bioactive RGD sites that promote cell adhesion and proliferation.[17−19] Gelatin hydrogels can be engineered through thermal gelation or chemical cross-linking to enhance their mechanical stability and support cellular interactions[20,21]. Both alginate and gelatin, with their natural origins, offer excellent biocompatibility and closely mimic the ECM, thus fostering superior cell attachment and growth compared with many synthetic alternatives. The ability of alginate to be functionalized with bioactive molecules further augments its role in tissue regeneration by directing specific cellular responses, while gelatin supports a conducive environment for cellular repair and regeneration.[22,23]

The controlled degradation rates of alginate and gelatin through ionic interactions for alginate and enzymatic activity for gelatin ensure that scaffolds degrade in harmony with tissue formation and remodeling. This optimal combination of mechanical support, bioactivity, and degradation control makes alginate−gelatin-based hydrogels particularly effective for complex soft tissue engineering. They address many of the limitations associated with synthetic and other natural hydrogels, advancing the field of regenerative medicine by providing scaffolds that closely mimic the native ECM, support tissue repair, and facilitate regeneration in complex soft tissue environments.[24] While extensive research has focused on the *in vitro* biocompatibility and various biophysical properties of alginate−gelatin hydrogel-based scaffolds, there is a notable gap in studies addressing their antimicrobial properties. This aspect is particularly crucial for regenerating complex soft tissues, such as urinary tissue, which is highly susceptible to bacterial infections.[25,26]

The alginate−gelatin-based hydrogels are hypothesized to enhance both antimicrobial efficacy and biophysical properties such as mechanical stiffness, viscoelastic properties, swelling, and degradation.[27,28] It is expected that nHAp, due to its nanoscale size and surface properties, interacts with bacterial membranes, leading to ion exchange processes, such as the release of calcium and phosphate ions, which compromise bacterial cell wall integrity. This disruption, coupled with nHAp's ability to generate reactive oxygen species (ROS), induces oxidative stress, leading to antimicrobial properties, which are particularly valuable where infection prevention is critical, such as in wound healing or urological scaffolds.[29−31]

Among the spectrum of advanced manufacturing approaches, the extrusion-based 3D printing of hydrogels provides notable benefits in tissue engineering by offering precise control over scaffold design and material properties.[32,33] This method enables the fabrication of complex, patient-specific scaffolds that closely replicate native tissue structures, which is critical for successful tissue regeneration and integration. Through careful adjustment of printing parameters and hydrogel composition, the technique allows for fine-tuning of scaffold features such as porosity, mechanical strength, and degradation rates, optimizing the environment for cell growth and nutrient diffusion.[34] Furthermore, extrusion-based 3D printing facilitates the incorporation of functional elements like vascular networks or controlled-release drug delivery systems, enhancing the scaffold's overall effectiveness. Its scalability makes it a viable and efficient method for producing customized, high-performance scaffolds suitable for a wide range of clinical applications.[34,35]

In this study, we develop nanohydroxyapatite-reinforced 3% alginate, 5% gelatin hydrogels (3A5G), focusing on the tunable biophysical properties, such as extent of swelling, degradation rate, mechanical strength, and rheological properties, etc. The nanohydroxyapatite-reinforced ink of all compositions (3A5G0.25H, 3A5G0.5H, and 3A5G0.75H) demonstrated good printability, and the buildability was established by making a circular matrix-shaped graft of different infill densities that could behave as a natural ECM. The disc-shaped graft of 62 layers and 2 cm height was successfully 3D-printed. Moreover, focusing on the future clinical translatability by producing a bulk number of coupon-sized samples for preclinical testing, a successful trial has been made regarding the direct printing of the ink in a cell culture well plate. A comprehensive understanding of the volumetric porosity of the pre-cross-linked hydrogel ink and 3D-printed graft was developed by the micro-CT analysis, where several pore characteristics such as pore volume fraction, pore interconnectivity, and pore tortuosity were analyzed by Amira Avizo software. Additionally, our study thoroughly investigates the antimicrobial properties of the nanohydroxyapatite-reinforced alginate−gelatin-based grafts against Gram-negative *Escherichia coli* and Gram-positive *Staphylococcus aureus* bacteria, where significant reduction in the bacterial adhesion was observed at higher concentration of nHAP in the hydrogel matrix.

2. MATERIALS AND METHODS

Pharmaceutical-grade sodium alginate was sourced from S D Fine Chem Limited (SDFCL). Nanohydroxyapatite, with a particle size of <200 nm (BET) with a purity of ≥97%, was purchased from Sigma-Aldrich. Gelatin derived from porcine skin (bloom strength ∼300) was also acquired from Sigma-Aldrich. The cross-linking agent utilized in the study, calcium chloride dihydrate ($CaCl_2{\cdot}6H_2O$), was obtained from Sigma-Aldrich.

2.1. Scanning Electron Microscopy (SEM). The morphology of the obtained nanohydroxyapatite (nHAp) was examined by using field emission scanning electron microscopy (ZEISS, ULTRA55). The samples were coated with a thin layer of gold via sputtering before analysis. To prepare the samples, a diluted dispersion of nHAp was drop-cast onto conductive carbon tape adhered to a metallic substrate. Subsequently, the samples were dried overnight in an oven.

2.2. Formulation of Nanohydroxyapatite-Reinforced Alginate/Gelatin-Based Hydrogel Ink. For synthesizing the alginate/gelatin/nanohydroxyapatite (nHAp)-based hydrogel, a different approach was employed. Initially, gelatin (*X*% w/v) was dissolved in water at 45 °C until a homogeneous solution was formed. Next, nanohydroxyapatite (nHAp) at varying concentrations (*Y*% w/v) was dispersed into the gelatin solution with continuous agitation at 45 °C until a uniform dispersion was obtained. This sequence was important because adding alginate before nHAp would have resulted in a highly viscous solution, making it difficult to achieve a uniform dispersion of the nanoparticles. Once the nHAp dispersion was ready, a predetermined amount of alginate (*Z*% w/v) was added to the nHAp−gelatin solution at 39 °C. The mixture was stirred overnight to form a semiviscous, homogeneous solution of alginate, gelatin, and nHAp. To facilitate gelation, both the alginate/gelatin (AG) and alginate/gelatin/nHAp-based hydrogels were refrigerated at 4 °C overnight, ensuring the formation of stable gel structures in both formulations.

2.3. Rheological Parameter Analysis. To ensure the synthesis of a hydrogel ink suitable for 3D printing with

https://doi.org/10.1021/acsomega.4c10743
ACS Omega 2025, 10, 18428−18443

favorable buildability, a range of rheological parameters were evaluated, including shear-thinning behavior, temperature- and frequency-dependent variations in storage modulus (G') and loss modulus (G''), linear viscoelastic regime (LVR), thixotropic characteristics, and the stability of pre-cross-linked hydrogel ink over time and temperature, particularly at physiological conditions. The rheological tests were conducted using an Anton Paar rheometer (Model-MCR 302) equipped with a 25 mm parallel plate configuration. Hydrogel samples were carefully placed between the plates at 21 °C, maintaining a 1 mm gap between them.

Initially, the viscoelastic properties of the hydrogel ink were assessed by varying the frequency from 0.01 to 100 rad/s, focusing on the storage (G') and loss modulus (G''). Gel stability was evaluated by measuring the temperature-dependent variations in G' and G'' across a range of 25−42 °C, with the upper limit exceeding physiological temperature (37 °C). Time-dependent stability of the pre-cross-linked hydrogel at room temperature was further analyzed through a time sweep, where changes in G' and G'' were monitored over 4 h at a constant shear strain of 1% and a fixed angular frequency of 1 rad/s. The linear viscoelastic regime was determined by applying a shear strain range of 0.1−1000%.

The hydrogel's shear-thinning behavior, or pseudoplasticity, was investigated by measuring viscosity variations across a shear rate range of 0.1−100 s^{-1}. Additionally, thixotropic analysis was performed to examine the hydrogel's shape recoverability in three stages: preprinting (Step I), during printing (Step II), and postprinting (Step III). In Step I, a shear rate of 0.1 s^{-1} was applied for 60 s. During Step II, a maximum shear rate of 100 s^{-1} was applied for 20 s, and in Step III, the initial shear rate of 0.1 s^{-1} was reapplied for 60 s. This method provided a detailed evaluation of the hydrogel's viscosity recovery throughout different stages of the printing process.

2.4. 3D Extrusion Printing of the Graft. To fabricate clinically applicable 3D-printed matrix-shaped grafts, a filament extrudability test was conducted, leading to the selection of a 22G nozzle for the final printing process. The extrusion pressure for each composition was then optimized by adjusting the flow rates for the selected material. A CAD design for the grafts was created by using SolidWorks 2022 software to fabricate circular matrix-shaped grafts having dimensions of 30 mm in diameter and 1 cm in height. To establish the buildability of the synthesized hydrogel ink further in terms of printing the structure of a larger height, a disc-shaped graft of 15 mm diameter and 2 cm height was designed by SolidWorks.

The design was exported as an STL file, which was then sliced by using Mito Plus software with a layer height of 0.4 mm. The printability and buildability of the synthesized hydrogel-based biomaterial ink were validated by using a custom-made extrusion printer developed by Avay Biosciences Pvt. Ltd., Bangalore, India. The printing was optimized at a temperature of 21 °C and a speed of 6 mm/s.

2.4.1. Postprinting Cross-Linking the Graft. Following the printing process, each structure underwent a cross-linking procedure using a 1 M calcium chloride ($CaCl_2$) solution to enhance the mechanical stability of the constructs. The printed structures were placed in a glass Petri dish, and a 1 M $CaCl_2$ solution was carefully applied drop by drop using a 20 mL plastic syringe. Afterward, the entire printed structure was fully submerged in a 1 M $CaCl_2$ solution for several hours to ensure thorough cross-linking. This step was essential to achieving the desired mechanical integrity and stability of the printed hydrogel constructs.

2.5. Physicochemical Characterizations. *2.5.1. FT-IR.* Fourier Transform Infrared (FT-IR) measurements were performed on cross-linked hydrogel-based grafts, both pre- and postimplantation, using a PerkinElmer spectrophotometer. The analysis was conducted over a wavelength range of 600−4000 cm^{-1} with a resolution of 4.0 cm^{-1}. Each sample underwent 32 scans to ensure accurate results. To eliminate moisture interference, all samples were thoroughly dried and stored in a desiccator overnight before the analysis.

2.5.2. TGA Analysis. To assess the thermal stability of the freeze-dried cross-linked hydrogel-based grafts, including the physiological temperature range, thermogravimetric analysis (TGA) was conducted. Samples weighing approximately 15−20 mg were placed in an alumina crucible for the analysis. The temperature range was set from room temperature (25 °C) to 700 °C, with a heating rate of 10 °C/min under a nitrogen atmosphere. The weight loss was recorded as a function of temperature, and derivative thermogravimetry (DTG) curves were generated to identify the material's thermal degradation stages.

2.6. Evaluation of the Mechanical Strength of Composite Hydrogel Scaffolds. *2.6.1. Compressive Strength.* To evaluate the compressive strength, cylindrical disc-shaped 3D-printed cross-linked samples were prepared for each composition, with dimensions of 15 mm in diameter, 10 mm in height, and an infill density of 20%. The samples were washed and immersed in PBS for 30 min to remove any residual $CaCl_2$. The compressive strength of each sample was measured using a microUTM analyzer (Mecmesin MultiTest-10-i) fitted with a 500 N load cell, operating at a cross-head speed of 2 mm/min. During testing, load−displacement data were collected for each sample. These data were then processed, using known dimensions (cross-sectional area and height) of the samples, to produce stress−strain curves. The compressive strength of the hydrogel scaffold was determined by analyzing these curves. Understanding the compressive strength is essential for assessing the scaffold's capacity to withstand compressive forces, a critical factor for its potential use in tissue engineering. Achieving compressive strength comparable to that of native tissue is key for the scaffold to provide adequate mechanical support for tissue regeneration.

2.7. Biophysical Properties. *2.7.1. Swelling.* The swelling capacity of hydrogels is a key factor in their suitability for 3D bioprinting and tissue engineering, as it reflects the hydrophilic nature of their three-dimensional polymeric network.[36,37] To assess this property, we cast hydrogel solutions of each composition into hollow cylindrical glass molds with an internal diameter of 10 mm and a height of 5 mm. The molds were placed at 4 °C for gelation, followed by cross-linking in 1 M $CaCl_2$ for several hours. For accuracy, 10 samples per composition were prepared. Afterward, the samples were freeze-dried for 24 h to remove excess water, and the dry weight of each disc was recorded as W_0.

To evaluate swelling efficiency, a measured volume of phosphate-buffered saline (PBS) was added to each sample, and the wet weight was recorded at time intervals of 0, 2, 4, 8, 12, 24, 48, and 72 h. At each time point, the samples were removed from the well plate, the surface water was gently blotted using tissue paper, and the wet weight was recorded as W_t. The swelling efficiency of each scaffold was calculated using the formula

https://doi.org/10.1021/acsomega.4c10743
ACS Omega 2025, 10, 18428−18443

$$\text{swelling efficiency (\%)} = (W_t - W_0/W_0) \times 100$$

This analysis provided valuable insights into the hydrogels' swelling behavior under physiological conditions over time.

2.7.2. Degradation Study. Enzymatic degradation assays were conducted on the hydrogel-based grafts using disc-shaped samples following a procedure similar to the swelling study. The cross-linked hydrogel samples were immersed in a PBS solution containing collagenase type I enzyme at a concentration of 2 U/mL and incubated at 37 °C. The remaining mass of the samples (M_t) was measured at various time points, including 0, 4, 5, 7, 9, 12, 15, 20, and 28 days after lyophilization. The percentage of residual mass was calculated relative to the initial dry weight (M_0) of the samples using the formula

$$\text{percentage of residual mass (\%)} = (W_t/W_0) \times 100$$

This analysis provided an assessment of the enzymatic degradation behavior of the hydrogel-based grafts over time. By tracking changes in mass, the study offered valuable insights into the degradation kinetics and stability of the grafts, which are essential for their application in tissue engineering.

2.8. Micro-CT Analysis: 3D Volumetric Microstructure of Pre-Cross-Linked Hydrogel Ink and Cross-Linked-3D-Printed Hydrogel-Based Graft. To examine the 3D porous structure of both freeze-dried pre-cross-linked hydrogel-based ink and post-cross-linked 3D-printed nanohydroxyapatite-based grafts (3A5G0.25H, 3A5G0.5H, 3A5G0.75H), micro-CT scanning was conducted with an Xradia Versa XRM 500. The resulting data were analyzed using Avizo software (Version 9.22). Samples were securely positioned on a specialized holder within the Xradia chamber, with careful adjustments to the X-ray source, detector, exposure time, and voltage to ensure a uniform intensity across specimens. Each sample underwent 2 h of 3D scanning session, producing 1601 projections per sample, based on the parameters specified in Figure 5.

After scanning, the data were reviewed with the TXM 3D viewer, and 2D orthoslices were visualized. The 3D porous structures, including pore volume fraction and interconnectivity, were analyzed by using Amira Avizo software (Thermo Fisher Scientific). The TXM files were processed to generate 2D orthoslices in three planes (XY, YZ, and ZX), and a 3D subvolume, designated as the volume of interest (VOI), was extracted for detailed analysis.

To distinguish pores from the hydrogel matrix, autothresholding was employed, and axis connectivity was assessed to determine the pore volume fraction. Pore spaces were isolated, and a pore network model was created based on the pore equivalent radius (EqRadius). Pore dimensions and histograms were analyzed through label analysis after thresholding and separation of the pores using interactive thresholding, opening, and separation modules. Additionally, the pore tortuosity was calculated using the centroid sphere tortuosity module within the axis connectivity analysis.

2.9. Bacterial Culture Studies. To evaluate the antimicrobial properties of the hydrogels, we utilized both Gram-positive *Staphylococcus aureus* (*S. aureus*) and Gram-negative *Escherichia coli* (*E. coli*) bacterial strains. Methicillin-resistant *S. aureus* (MRSA, USA 300) was sourced from the Sir Dorabji Tata Centre for Research in Tropical Diseases, Bangalore, while wild-type *E. coli* (K12 MG 1655) was obtained from the National Centre for Biological Sciences (NCBS). The glycerol stock of *S. aureus* was revived on Tryptic Soy Agar, and *E. coli* was revived on Nutrient Agar. Single colonies from the agar plates were inoculated into 5 mL of Tryptic Soy Broth for *S. aureus* and Luria Broth for *E. coli* and incubated overnight at 37 °C with constant shaking at 100 rpm. The following morning, the optical density was measured using a spectrophotometer, and the culture was adjusted to 0.5 OD to ensure it was in the log phase.

Hydrogel samples were cut into 1 cm^2 pieces, sterilized by immersion in 100% ethanol, and exposed to UV light for 1 h. After sterilization, the samples were thoroughly washed with 1× PBS and placed in duplicate wells of a 12-well plate. Each well received 1 mL of the bacterial culture and was incubated for 4 h.

2.9.1. Serial Dilution and Plating. Following a 4 h incubation period, a serial dilution was performed. 1 mL of the bacterial suspension from each well was transferred to 9 mL of fresh Tryptic Soy (TS) or Luria Broth (LB), depending on the bacterial strain. This suspension was then subjected to serial dilution up to a 10^{-9} dilution factor. From the last four dilutions, 100 μL of each was plated on Tryptic Soy Agar (for *S. aureus*) or Nutrient Agar (for *E. coli*). The plates were incubated overnight at 37 °C. The next morning, colonies were counted to determine the colony-forming units (CFUs) and extrapolated to the original volume.

The outcome of this study was represented by calculating the log reduction in the number of CFUs/mL and determining the percentage reduction

$$\text{No. of CFU/mL} = \frac{\text{No. of colonies}}{\text{volume of dilution plates} \times \text{dilution factor}}$$

$$\text{log 10 CFU reduction CFU/mL} = \frac{\text{No of CFU/mL in control}}{\text{No of CFU/mL in treated culture}}$$

2.9.2. Fluorescence Confocal Microscopy: Live Bacteria. To assess the antimicrobial property on a qualitative and quantitative basis, live staining of the bacteria on the hydrogel surface was done. The live stain was prepared according to the Kit instructions for the LIVE/DEAD Viability/Cytotoxicity Kit* from Thermo Fisher Scientific.

Living cells are identified by their internal esterase activity, which converts the cell-permeant calcein AM into fluorescent calcein. Calcein, a negatively charged dye, remains within live cells, emitting a strong green fluorescence (~495 nm excitation/~515 nm emission). After removal of the bacterial suspension from the hydrogel, it was washed with PBS mildly and 1 mL of the live stain was added and incubated in the dark for 40 min. After 40 min, the stain was removed, and the material was transferred to a glass slide for a confocal microscope. The images were taken with an FITC filter. Intensity was quantified on the ImageJ software and normalized with respect to the range.

2.9.3. Mammalian Cell Culture. For mammalian cell culture, DMEM stock media was supplemented with 10% (v/v) FBS and an antibacterial-antimycotic solution (Thermo Fisher) following the manufacturer's instructions, mixed aseptically, filter-sterilized, stored at 4 °C, and warmed to 37 °C before use. NIH-3T3 fibroblast cells, isolated from a Swiss mouse embryo, were thawed at room temperature, resuspended in 1 mL of working media, centrifuged at 2000 rpm for

https://doi.org/10.1021/acsomega.4c10743
ACS Omega 2025, 10, 18428−18443

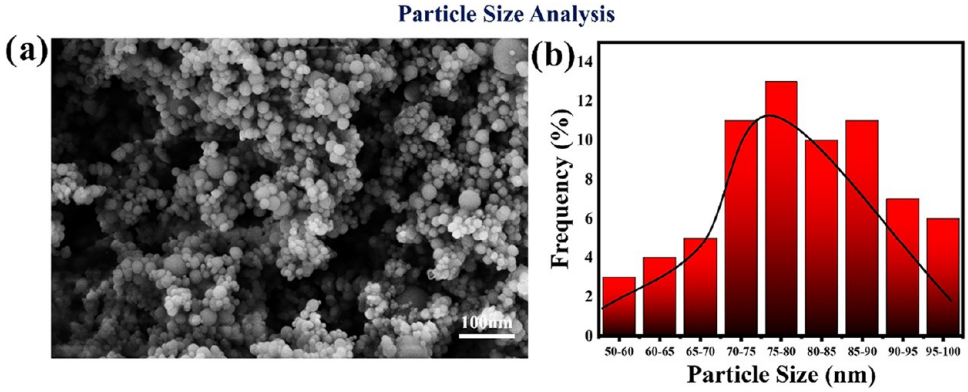

Figure 1. (a) SEM images of nanohydroxyapatite powder particles. (b) The obtained particle size distribution from the SEM images calculated by ImageJ software.

7 min, and the pellet was resuspended in fresh media. The suspension was transferred to a T-25 or T-75 flask with 3 or 7 ml working media and incubated at 37 °C in 5% CO_2. At a 70% confluence, cells were trypsinized, centrifuged, and resuspended in 1 mL of fresh media. A total of 100,000 cells were seeded onto hydrogels sterilized for 4 h with 70% ethanol under UV light, with 500 μL of media added to each well.

2.9.3.1. WST-1 Assay. Cell viability on cross-linked hydrogel samples was assessed at 3, 5, and 7 days using the WST-1 assay, which measures the mitochondrial activity. At each time point, the growth medium was aspirated, and samples were washed with 1× PBS to remove nonadherent cells. A 500 μL solution of 10% WST-1 in DMEM was added to each well and incubated at 37 °C for 2 h. The reduction of WST-1 to formazan by mitochondrial dehydrogenase activity in viable cells produced a color change, and absorbance was measured at 450 nm by using a microplate reader (AF2200, Eppendorf). Cell viability was calculated as a percentage of the control using the following equation

$$\%\ \text{cell viability} = (\text{absorbance of sample} / \text{absorbance of control}) \times 100$$

2.9.3.2. Confocal Microscopy. Hydrogel samples were cultured in the appropriate media for 3 days, after which they were prepared for confocal imaging. On day 3, the samples were washed three times with 1× phosphate-buffered saline (PBS) and fixed with 2% paraformaldehyde (PFA) for 45 min at room temperature to preserve cellular structures. Following fixation, the samples were permeabilized with 0.1% Triton X-100 in PBS for 5 min and washed three times with PBS to remove excess detergent. Alexa Fluor 488 Phalloidin, diluted according to the manufacturer's instructions (Thermo Fisher), was applied to stain F-actin filaments, with overnight incubation at 4 °C. After staining, the samples were washed three times with PBS to remove unbound dye, followed by nuclear staining using DAPI (4′,6-diamidino-2-phenylindole) for 10 min at room temperature. Excess DAPI was removed with three additional PBS washes. The stained samples were mounted on glass slides using an appropriate mounting medium, and high-resolution images were acquired using an Olympus Confocal Microscope at 20× magnification with optimized excitation/emission settings for Alexa Fluor 488 (green) and DAPI (blue).

2.10. Statistical Analysis. Statistical analysis was conducted using one-way ANOVA, followed by Tukey's post hoc analysis, utilizing GraphPad Prism Version 8.0.2 (263). A significance level of $p \leq 0.05$ was established, with all analyses performed in triplicate ($n = 3$). Error bars in the graphs represent the standard deviation derived from the mean values.

3. RESULTS AND DISCUSSION

In tissue engineering, the nanohydroxyapatite-based hydrogel formulations and scaffolds have been extensively explored, particularly for bone and cartilage tissue engineering.[38,39] However, the nanohydroxyapatite-based scaffolds could be highly effective for soft tissue engineering due to their good biocompatibility, mechanical strength, and antimicrobial properties.[40,41] Moreover, due to its Ca^{2+} and PO_4^{3-} contents, it could significantly promote mineralization, which is highly effective for any kind of soft tissue engineering.[42−45] The following sections provide a comprehensive idea regarding the tunability of several biophysical and physicochemical properties of the alginate−gelatin-based hydrogel ink and 3D-printed scaffolds by varying the concentration of nHAP. Moreover, an effective way of improving the antimicrobial property of the 3D-printed hydrogel scaffolds by varying the concentration of nHAP is also presented in this section. The SEM morphological investigation of the nHAP powder showed a completely uniform spherical-shaped particle distribution, as shown in Figure 1.

3.1. Synthesis of Homogeneously Formed Nanohydroxyapatite-Reinforced Hydrogel-Based Biomaterial Ink. The sequential mixing of the three components of the hydrogel at a specific temperature and mixing condition results in the formation of a homogeneous white-colored hydrogel, which is crucial for the smooth extrusion of filaments from the printing cartridge [Figure 2a,b]. The concentration of nanohydroxyapatite (nHAp) was varied within a small range from 0.25 to 0.75%. It was observed that when the nHAp concentration was below 0.25%, the gel stability was poor, likely due to insufficient interconnectivity and interparticle interaction at low concentrations below the percolation threshold. Optimal printability and physicochemical properties were achieved within this narrow concentration range, while at concentrations higher than 0.75%, the hydrogel's viscosity became too high for 3D printing, preventing further improvement of biophysical properties [Table 1].

3.2. Physicochemical Interactions of the 3D-Printed Graft. *3.2.1. FT-IR.* The chemical interactions between the

https://doi.org/10.1021/acsomega.4c10743
ACS Omega 2025, 10, 18428−18443

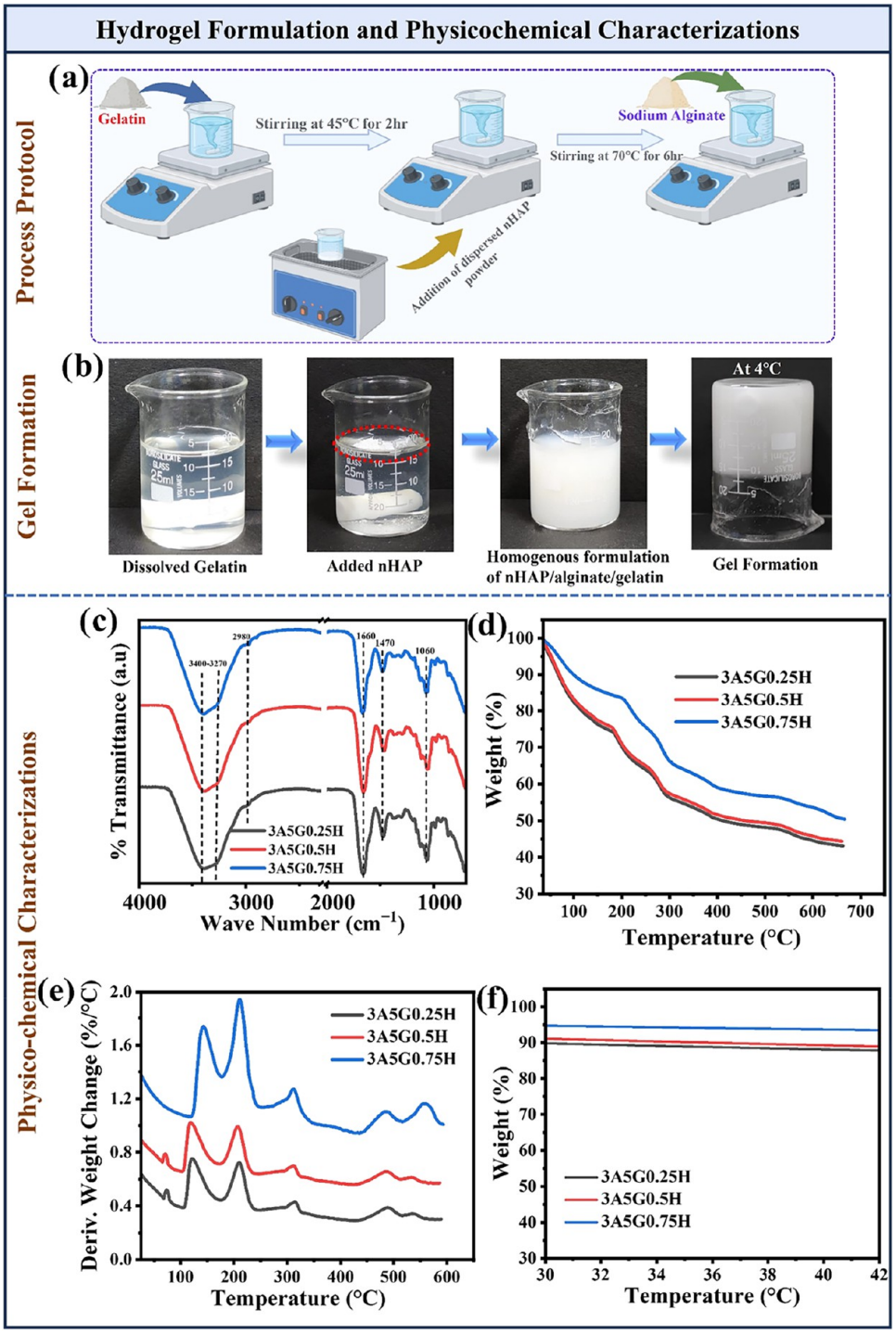

Figure 2. Representation of the overall procedure of formulation of the homogeneous nanohydroxyapatite-reinforced alginate−gelatin-based hydrogel and several physicochemical characterizations. (a) Schematic represents the formulation steps of the homogeneous hydrogel ink [created by Biorender.com]. (b) The homogeneous dispersion of nanohydroxyapatite in the hydrogel matrix and the formulation of the stable homogeneous hydrogel at 4 °C. (c) FT-IR analysis of the synthesized freeze-dried cross-linked hydrogel ink to understand the extensive physicochemical interactions between the components. (d) Measurement of thermal stability of the freeze-dried cross-linked hydrogel ink through the change of weight percentage with respect to temperature by TGA analysis. (e) Differential thermogram defines the maximum weight loss temperature of the cross-linked hydrogel-based grafts. (f) The stability of the cross-linked hydrogel-based graft in the physiological temperature window by TGA.

components of the nHAp-based hydrogel compositions were analyzed using FT-IR spectroscopy on 3D-printed cross-linked scaffolds. Since the primary components of all three different compositional variations (3A5G0.25H, 3A5G0.5H, and 3A5G0.75H) are similar, overlapping of characteristic peaks in the FT-IR spectra was observed. However, IR bands appearing at 1004−1013 and 1060−1083 cm^{-1} correspond to the C−C and C−O stretching vibrations of alginate [Figure 2c]. The broad IR bands observed at 1674 and 1470 cm^{-1} correspond to the asymmetric and symmetric stretching vibrations of the carboxylate ion (COO^-) of alginate, indicating the formation of adequately cross-linked hydrogel

https://doi.org/10.1021/acsomega.4c10743
ACS Omega 2025, 10, 18428−18443

Table 1. Formulated Hydrogel-Based Compositions with Respect to Different Concentrations of Nanohydroxyapatite (nHAP)

hydrogel composition	alginate X%	nanohydroxyapatite (nHAP), Y%	gelatin, Z%
3A5G0.25H	3	0.25	5
3A5G0.5H	3	0.5	5
3A5G0.75H	3	0.75	5

scaffolds. The IR band at 1674 cm^{-1} also corresponds to the amide I band and the C−O and C−N stretching bonds of gelatin. The characteristic peaks of nHAp include those at 962 and 1040−1080 cm^{-1}, which are attributed to the phosphate (PO_4^{3-}) group stretching vibration. Additionally, the IR bands at 1532 and 1236 cm^{-1} correspond to gelatin's amide II and amide III stretching vibrations of the C−N and N−H groups, respectively. The broad peak for the O−H group appears at 3400−3270 cm^{-1}, and the C−H stretching is observed at 2980 cm^{-1} [Figure 1c].

3.2.2. TGA. To investigate the thermal stability of the 3D-printed hydrogel-based graft within a temperature range that includes physiological conditions, thermogravimetric analysis (TGA) was performed. Thermal degradation is typically identified by a weight loss of 5−10%, which often indicates the onset of significant material decomposition. For certain polymers and biomaterials, a 5% weight loss (termed T_s) is used as an indicator of degradation onset. In this study, the T_s values for 3A5G0.25H, 3A5G0.5H, and 3A5G0.75H are 51, 51, and 74 °C, respectively [Figure 2d]. The differential thermogram curve represents the rate of weight loss as a function of temperature (or time) derived by taking the derivative of the weight loss curve. The temperature at the peak maximum is reported as the maximum degradation temperature (T_{max}), indicating when the material degrades at its fastest rate. The T_{max} values for 3A5G0.25H, 3A5G0.5H, and 3A5G0.75H are 119, 119, and 143 °C, respectively [Figure 2e]. At higher concentration of nanohydroxyapatite (nHAp) in the cross-linked hydrogel matrix (3A5G0.75H), the thermal stability was significantly improved, as evidenced by TGA and DTG data. The TGA analysis could not reveal any significant degradation of the cross-linked hydrogel-based grafts at physiological temperature, and hence no significant deviation from the linearity was noticed within the physiological temperature window [Figure 2f].

3.3. Rheological Property Analysis. The rheological evaluation of nanohydroxyapatite (nHAp)-reinforced alginate−gelatin-based hydrogel scaffolds is crucial, as it provides key insights into the material's mechanical behavior, processability, and suitability for tissue engineering.[46,47] Rheological properties, such as viscoelasticity (storage and loss moduli), shear-thinning behavior, and gelation kinetics, help to predict how the hydrogel will perform under physiological conditions.

3.3.1. Shear-Thinning Behavior. The shear-thinning nature of nHAp−alginate−gelatin hydrogels facilitates smooth extrusion and maintains shape fidelity in 3D printing.[48] The initial viscosity for 3A5G0.25H, 3A5G0.5H, and 3A5G0.75H was 3.8×10^5, 5.6×10^5, and 1.0×10^6 mPa.s, respectively, at a shear rate of 0.1 (1/s), within the optimal range for extrusion printing ($30-6 \times 10^7$ mPa·s).[49] The viscosity vs shear rate plot [Figure 3b] showed a continuous decrease in viscosity with increasing shear rate, confirming shear-thinning behavior. Additionally, the increasing nHAp concentration led to a gradual increase in zero-shear viscosity, attributed to the formation of a restrictive network that limits polymer chain flow [Figure 3a].

3.3.2. Linear Viscoelastic Regime. The influence of shear on the gel properties was analyzed through amplitude sweep tests, focusing on the effect of varying nanohydroxyapatite (nHAp) concentrations in the hydrogel matrix. The viscoelastic behavior within the linear viscoelastic regime (LVR) was assessed by varying shear strain from 0.01 to 1000 rad/s and shear stress from 0.1 to 1000 Pa. For all compositions, the storage modulus (G') exceeded the loss modulus (G''), with $\tan\delta$ values below 1 until the crossover region. The crossover for 3A5G0.25H occurred at 0.7% strain and 601 Pa, shifting to higher strain and stress for 3A5G0.5H (1.1%, 712 Pa) and 3A5G0.75H (1.02%, 721 Pa) [Figure 3c,d]. The addition of nHAp reduced gel deformability under shear stress due to enhanced intermolecular interactions from the high surface area of the nanoparticles.

As shear strain increased, yielding occurred with G'' surpassing G'. Beyond the crossover, permanent deformation and gel structure breakdown led to $\tan\delta$ values exceeding 1. The $\tan\delta$ crossover regions for 3A5G0.25H, 3A5G0.5H, and 3A5G0.75H were at 0.71, 1.02, and 1.1% strain, respectively [Figure 3e], indicating stronger mechanical interlocking at higher nHAp concentrations and a shift of the crossover to higher strain.

3.3.3. Gel Strength. All hydrogel compositions (3A5G0.25H, 3A5G0.5H, and 3A5G0.75H) consistently showed a higher storage modulus (G') than loss modulus (G'') across the frequency range, indicating increased stiffness with nanohydroxyapatite (nHAp) [Figure 3f]. nHAp particles enhance G' through their high stiffness, reinforcing the matrix by transferring mechanical loads. Strong interfacial interactions between nHAp and polymer chains restrict chain mobility, reducing relaxation under stress. The high aspect ratio of nHAp increases stress transfer surface area, and at higher concentrations, nHAp forms a percolating network, further boosting stiffness and elastic response. Significant improvements in both G' and G'' were observed for 3A5G0.75H. Higher nHAp concentrations enhance adhesion between nHAp and the matrix, reducing polymer chain flexibility and increasing G'. The restricted polymer dynamics lead to higher energy dissipation, increasing G''. A notable reduction in the $\tan\delta$ value was observed as the nHAp concentration increased from 0.25 to 0.75% due to the formation of stronger percolating networks that improve stress transfer and amplify elasticity [Figure 3g].

3.3.4. Temperature-Dependent Stability of the Hydrogel Ink. Gel stability of all hydrogel compositions was assessed using a temperature sweep, monitoring viscosity, storage modulus (G'), and loss modulus (G'') with temperature. As temperature increased, the hydrogel chain mobility increased, leading to a decrease in G', G'', loss factor, and viscosity with minimal decrease until temperatures exceeded 30 °C. Beyond this point, G', G'', and viscosity declined steadily, indicating polymer chain disentanglement. For 3A5G0.25H, 3A5G0.5H, and 3A5G0.75H, the $\tan\delta$ value remained <1 up to temperatures of 37.4, 38.2, and >40 °C, respectively, indicating viscoelastic stability at physiological temperature (37 °C). Due to viscosity and modulus reductions above 30 °C, 3D printing should be conducted at temperatures below 30 °C [Figure 3h−j]. The higher nHAp concentration in 3A5G0.75H

https://doi.org/10.1021/acsomega.4c10743
ACS Omega 2025, 10, 18428−18443

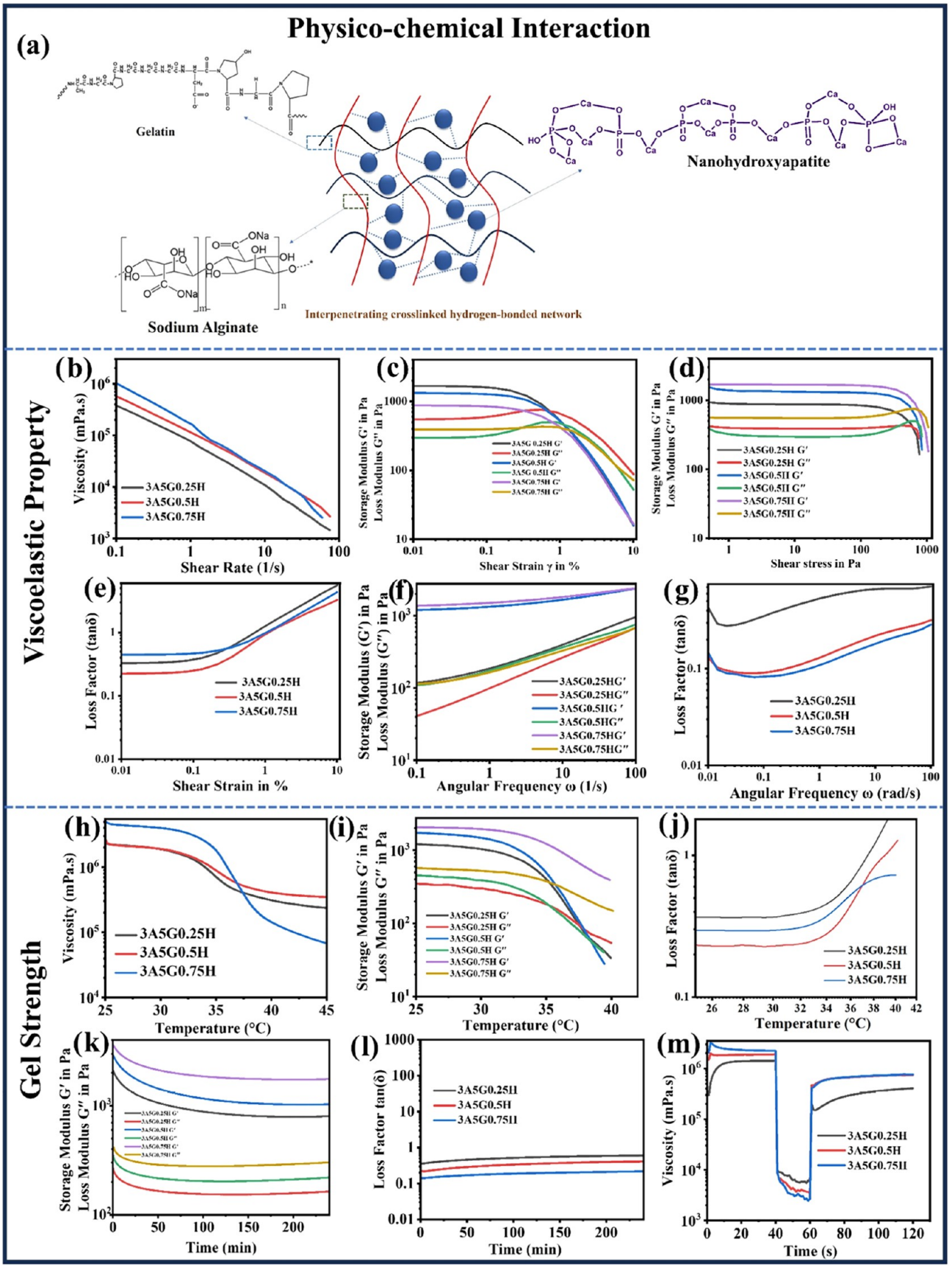

Figure 3. Analysis of the rheological properties and developing a correlation between the rheological properties of the hydrogel ink with intermolecular networking between the nanohydroxyapatite with alginate/gelatin. (a) The schematic represents the mechanical interlocking phenomenon inside the hydrogel-based components responsible for maintaining the pseudoplastic and viscoelastic properties of the hydrogel ink. (b) Pseudoplastic/shear-thinning behavior of the synthesized hydrogel ink. Panels (c−e) show the evaluation of the linear viscoelastic regime

https://doi.org/10.1021/acsomega.4c10743
ACS Omega 2025, 10, 18428−18443

Figure 3. continued

(LVR) of the hydrogel ink by amplitude sweep by observing the variation of storage modulus (G') and loss modulus (G''), with respect to shear stress and shear strain and to find the crossover region. (f, g) Analysis of the strength of the synthesized hydrogel ink through frequency sweep by observing the variation of storage modulus (G'), loss modulus (G''), and tanδ with respect to frequency. (h–j) Analysis of gel stability with respect to temperature by observing the variation of storage modulus (G'), loss modulus (G''), loss factor (tan δ), and viscosity with respect to temperature in a temperature window including the physiological temperature window. Panels (k, l) represent the evaluation of gel stability with respect to time by observing the linearity of storage modulus (G'), loss modulus (G''), and loss factor (tan δ) with respect to time up to 4 h. (m) The analysis of shape recoverability, i.e., the thixotropic behavior of the synthesized hydrogel ink.

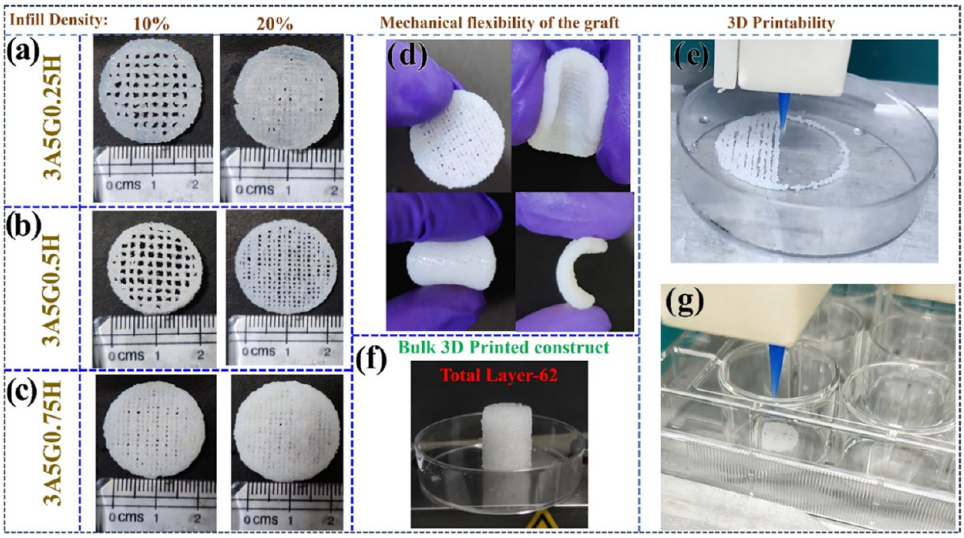

Figure 4. 3D extrusion printability and buildability of the synthesized hydrogel inks (3A5G0.25H, 3A5G0.5H, and 3A5G0.75H). Panels (a–c) represent the successfully fabricated matrix-shaped graft of different infill densities with a well-maintained pore integrity for all of the hydrogel-based compositions. (d) The flexibility, foldability, and stability of the matrix-shaped grafts are essential to mimic the viscoelastic property of the native tissue. Panels (e, g) represent the evidence of successful 3D printing on certain substrates like Petri dishes and cell culture well plates. (f) 3D buildability by the formation of bulk 3D construct up to 62 layers and 2 cm height.

enhanced thermal stability by improving interactions between nHAp particles and polymer chains. This interaction helps maintain structural integrity and prevents excessive disentanglement at elevated temperatures. The stable network created by nHAp allows the hydrogel to retain its mechanical properties and viscosity as temperature increases, particularly in physiological conditions.

3.3.5. Temporal Stability of the Hydrogel Ink. The synthesized hydrogel inks consistently exhibited a higher storage modulus (G') compared to the loss modulus (G''), with tan δ values remaining below 1 throughout the 4 h experimental period at room temperature (25 °C). The consistent linearity of G' and G'' indicates that the incorporation of nanohydroxyapatite (nHAp) enhances the hydrogel's ability to resist structural degradation over time [Figure 3k,l]. This stability under prolonged stress is crucial for maintaining the hydrogel's viscoelastic properties, which are essential for applications such as 3D printing and tissue engineering, where long-term mechanical performance is required.

3.3.6. Thixotropic Behavior. The low shear viscosities of 3A5G0.25H, 3A5G0.5H, and 3A5G0.75H were 8.7×10^5, 1.4×10^6, and 2.1×10^6 mPa·s, respectively, at a shear rate of 0.1 (1/s). During the test, viscosity remained linear at an initial shear rate of 0.1 (1/s) for 114 s, followed by an abrupt decrease at a maximum shear rate of 100 (1/s) for 5 s. Upon returning to the initial shear rate, the viscosity significantly recovered. The recoverable viscosities for 3A5G0.25H, 3A5G0.5H, and 3A5G0.75H were 4.0×10^5, 1.3×10^6, and 8.0×10^5 mPa·s, respectively. Notably, viscosity recovery was higher for 3A5G0.75H compared to those of 3A5G0.25H and 3A5G0.5H [Figure 3m].

The improvement of viscosity recovery at a higher concentration of nHAP in the hydrogel matrix (0.75%) could be attributed to the improved macromolecular interaction between 3A5G with nHAP as discussed before.

3.4. 3D Extrusion-Printed Grafts: Analysis of Printability. The study optimized key parameters for the 3D extrusion printing of nanohydroxyapatite (nHAp)-reinforced alginate–gelatin hydrogels (3A5G). Optimal printability was achieved with 3% alginate, 5% gelatin, and nHAp concentrations of 0.25–0.75 w/v%. Hydrogels with lower viscosity (e.g., 3A5G0.25H) required a lower printing pressure and temperature (19 °C), while those with higher viscosity (e.g., 3A5G0.75H) needed a higher pressure and temperature (21 °C) due to shear-thinning behavior. Printing speed (6 mm/s) and layer height (0.4 mm, ∼80% of the 22G nozzle size) were critical for precise filament formation and stable layers. Constructs, including circular matrix-shaped grafts (1 cm height, 6 mm inner diameter) with 10–20% infill [Figure 4a–c,e] and free-standing disc-shaped grafts (2 cm height, 62 layers) [Figure 4f], exhibited excellent pore integrity, flexibility, and shape fidelity. The successful printing of matrix-shaped grafts in a cell culture well plate demonstrated scalability for preclinical and clinical studies [Figure 4g]. These constructs

https://doi.org/10.1021/acsomega.4c10743
ACS Omega 2025, 10, 18428–18443

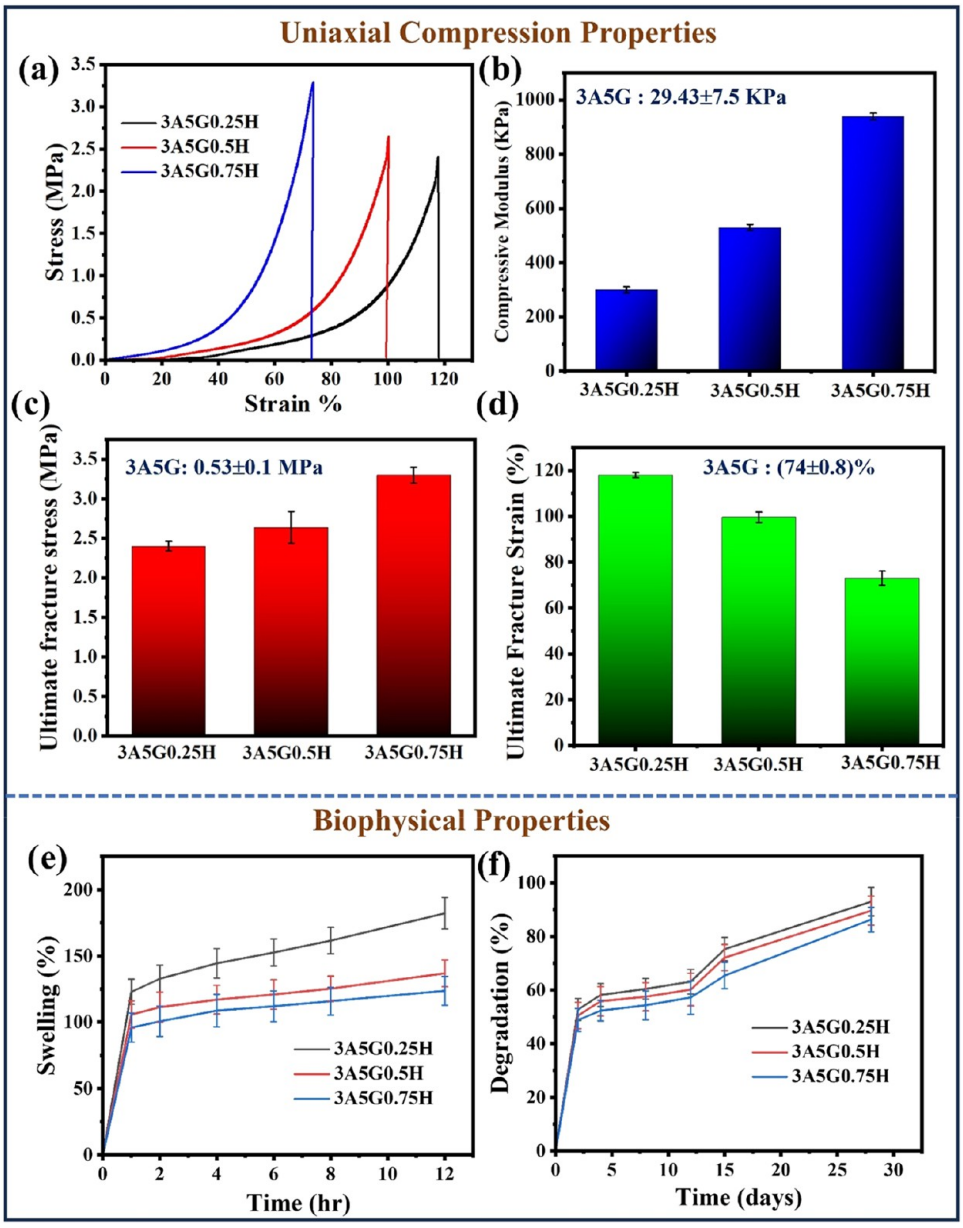

Figure 5. Evaluation of compressive strength and the biophysical properties of the 3D-printed nHAP-reinforced hydrogel scaffolds. Panel (a) represents the stress−strain curve obtained from the uniaxial compression test. Panels (b−d) are obtained from compressive modulus, fracture stress, and fracture strain, respectively. Panels (e, f) represent the percentage of swelling and degradation of the synthesized cross-linked freeze-dried hydrogel-based grafts with respect to time.

maintained pore stability, flexibility, and foldability [Figure 4d], mimicking native tissue characteristics effectively.

3.5. Uniaxial Compression. The compressive and tensile strengths of cross-linked hydrogel scaffolds were evaluated using uniaxial compression The ultimate compressive fracture strengths for 3A5G0.25H, 3A5G0.5H, and 3A5G0.75H were 2.4, 2.6, and 3.3 MPa, respectively, with compressive moduli of 299, 526, and 938 KPa and ultimate fracture strains of 118, 100, and 72% [Figure 5a−d].

The incorporation of nanohydroxyapatite (nHAp) led to a 3.13-fold increase in the compressive modulus, significantly enhancing the mechanical properties of 3D-printed alginate−gelatin-based scaffolds. Soft tissue-engineered hydrogel scaffolds, including those for cartilage, skin, and urinary tissue, generally exhibit compressive moduli between 10 and 800 kPa, with FDA-approved bioinks and cross-linked alginate- or gelatin-based scaffolds often falling within this range.[50,51] In this study, the highest-performing scaffold, 3A5G0.75H, demonstrated a compressive modulus of 938 kPa, exceeding this range while maintaining both printability and biocompatibility. Previous studies on nHAp-reinforced hydrogels have reported modulus improvements of 1.5−2.5-fold,[49,52] whereas the 3.13-fold increase observed here suggests a more efficient reinforcement mechanism, potentially due to optimized nHAp dispersion and enhanced cross-linking interactions. The resulting mechanical strength is particularly advantageous for applications requiring increased load-bearing capacity such as bladder and cartilage tissue engineering. Furthermore, the achieved modulus closely matches the native mechanical properties of urinary bladder tissue (200−800 kPa), highlighting its potential for clinical translation in complex soft tissue reconstruction.[52]

https://doi.org/10.1021/acsomega.4c10743
ACS Omega 2025, 10, 18428−18443

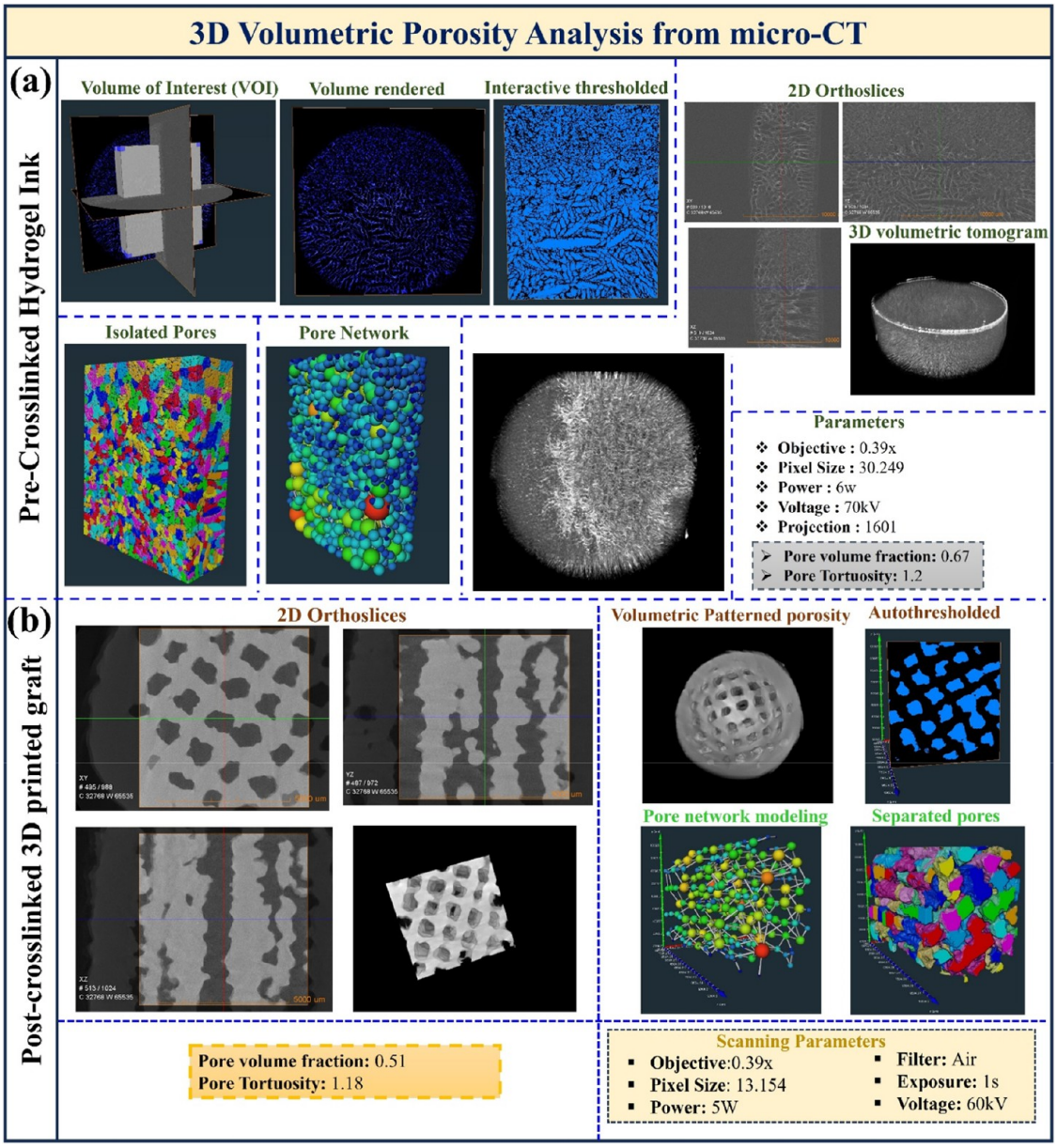

Figure 6. Analysis of 3D volumetric microstructure and porosity of different 3D-printed hydrogel-based grafts by micro-CT analysis. Panels (a, b) represent the 3D volumetric microstructure of pre-cross-linked hydrogel ink and cross-linked 3D-printed disc-shaped scaffolds, with 50 layers having a linear infill density at 0 and 90°. The volumetric porosity analysis was carried out by performing the computational analysis of the micro-CT data through Amira Avizo software to evaluate several parameters such as pore volume fraction, pore tortuosity, and pore interconnectivity.

3.6. Biophysical Properties. *3.6.1. Swelling.* Regulating the swelling behavior of hydrogel-based grafts is essential for maintaining mechanical integrity, preventing tissue damage, and optimizing cellular infiltration and nutrient diffusion, ensuring a favorable environment for tissue regeneration. An abrupt swelling increase was observed at 1 h, with percentages of 122, 105, and 95% for 3A5G0.25H, 3A5G0.5H, and 3A5G0.75H, respectively. Swelling continued to increase gradually up to 12 h, reaching 182, 136, and 123%, corresponding to 60, 31, and 28% increases relative to 1 h [Figure 5e]. Swelling initially occurs due to osmotic pressure from hydrophilic interactions, balanced at equilibrium by elastic forces within the cross-linked network. The decrease in swelling with an increasing nHAp content is attributed to the enhanced cross-linking density, reduced free volume, and the rigidity of nHAp, which collectively limit water uptake, hydrogel−water interactions, and polymer chain mobility, thereby reducing the percentage of swelling as the nHAp concentration increases.

3.6.2. Degradation Study. Regulating the degradation of hydrogel-based grafts is critical in tissue engineering to synchronize scaffold breakdown with tissue regeneration, ensuring mechanical support and a conducive environment for tissue integration and growth.[51,53] In this study, controlled degradation was observed for all scaffolds up to 30 days, with an abrupt increase at 5 days, a gradual increase until 20 days, and equilibrium thereafter. At 5 days, degradation percentages were 58, 55, and 52% for 3A5G0.25H, 3A5G0.5H, and 3A5G0.75H, respectively, with the highest degradation in 3A5G0.25H. By 30 days, degradation reached 93% for 3A5G0.25H, 89% for 3A5G0.5H, and 86% for 3A5G0.75H [Figure 5f]. Increasing the nHAp content enhances structural

https://doi.org/10.1021/acsomega.4c10743
ACS Omega 2025, 10, 18428−18443

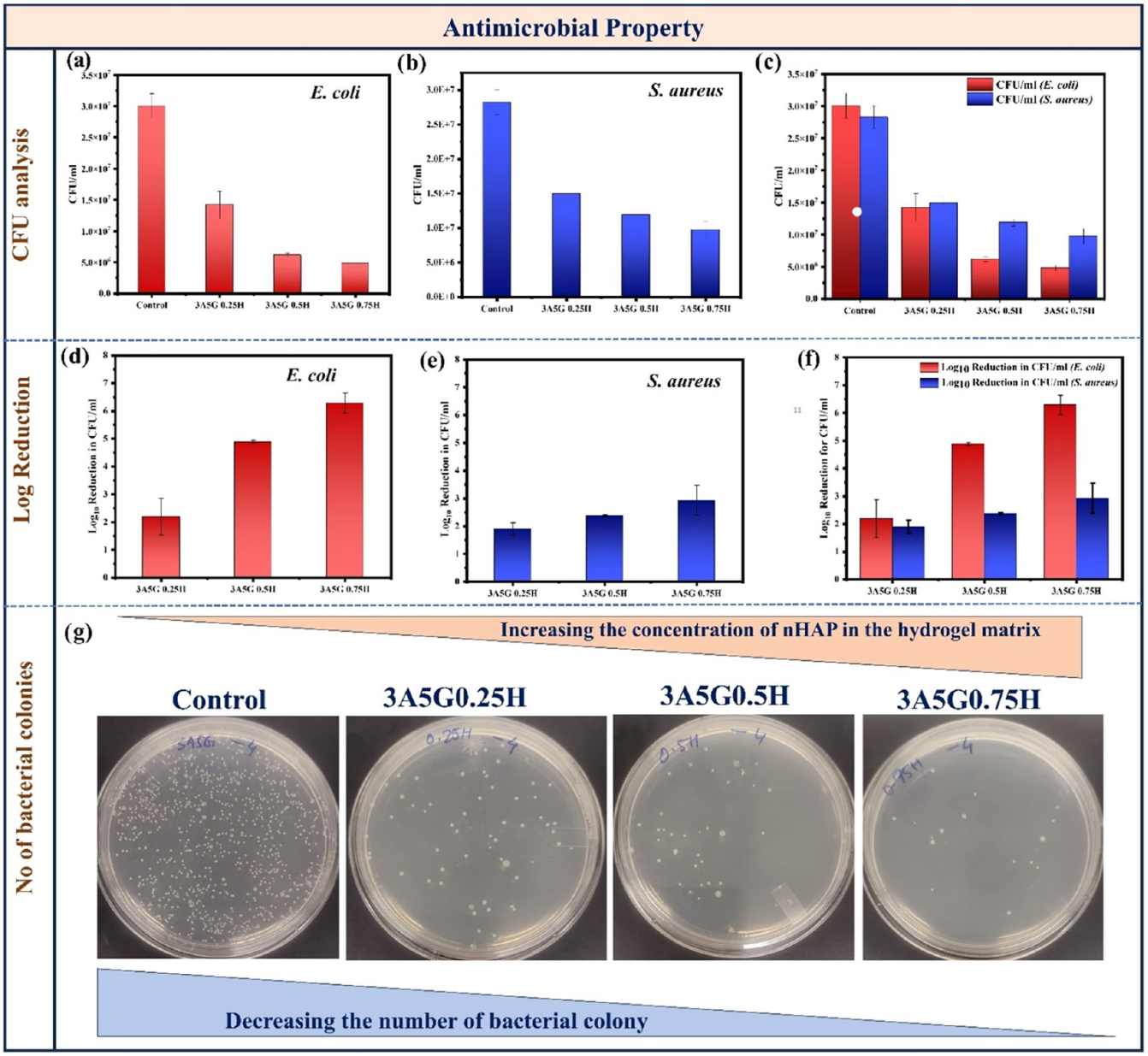

Figure 7. A comparative outcome analysis of the antimicrobial study analysis of the cross-linked hydrogel-based scaffolds 3A5G0.25H, 3A5G0.5H, and 3A5G0.75H with respect to Gram-negative *E. coli* and Gram-positive *S. aureus* bacteria. Panels (a−c) represent the obtained CFU results with respect to *E. coli* and *S. aureus* bacterial strain. Panel (c) represents the comparative understanding of the number of CFUs on the culture samples with respect to two different types of bacterial strain. Panels (d, e) represent the obtained log reduction from the CFU study, with respect to *E. coli* and *S. aureus* bacteria. Panel (f) represent the comparative understanding of the obtained log reductions on the cultured samples with respect to *E. coli* and *S. aureus* bacteria. Panel (g) represents the plate pictures of the CFU study performed on the cross-linked hydrogel surface of 3A5G0.25H, 3A5G0.5H, and 3A5G0.75H.

Table 2. Quantitative Outcome from the CFU Assay

hydrogel samples	*E. coli*		*S. aureus*	
	CFU/mL	$\log_{10}$ reduction	CFU/mL	$\log_{10}$ reduction
control	3.01×10^{07}	NA	2.83×10^{07}	NA
3A5G0.25H	1.42×10^{07}	2.2	1.50×10^{07}	1.9
3A5G0.2H	6.15×10^{06}	4.9	1.19×10^{07}	2.4
3A5G0.75H	4.80×10^{06}	6.3	9.75×10^{06}	2.8

integrity, reduces swelling, and limits the exposed surface area, mitigating localized stress and enzymatic or chemical attack. These factors collectively ensure controlled degradation, aligning the scaffold breakdown with tissue regeneration.

3.7. Micro-CT Analysis of the Hydrogel Scaffolds. For 3D-printed hydrogel scaffolds, the 3D microstructure plays a pivotal role in the biocompatibility. For example, a high pore volume fraction enhances cell infiltration and distribution, while the effective pore interconnectivity allows nutrients and oxygen to diffuse efficiently throughout the scaffold, which is crucial for forming a functional tissue matrix. Collectively, 3D microstructure-related features optimize the scaffold's capacity to support and enhance tissue growth.

To evaluate the 3D porous microarchitecture of the synthesized and 3D-printed hydrogel-based grafts, micro-CT

https://doi.org/10.1021/acsomega.4c10743
ACS Omega 2025, 10, 18428−18443

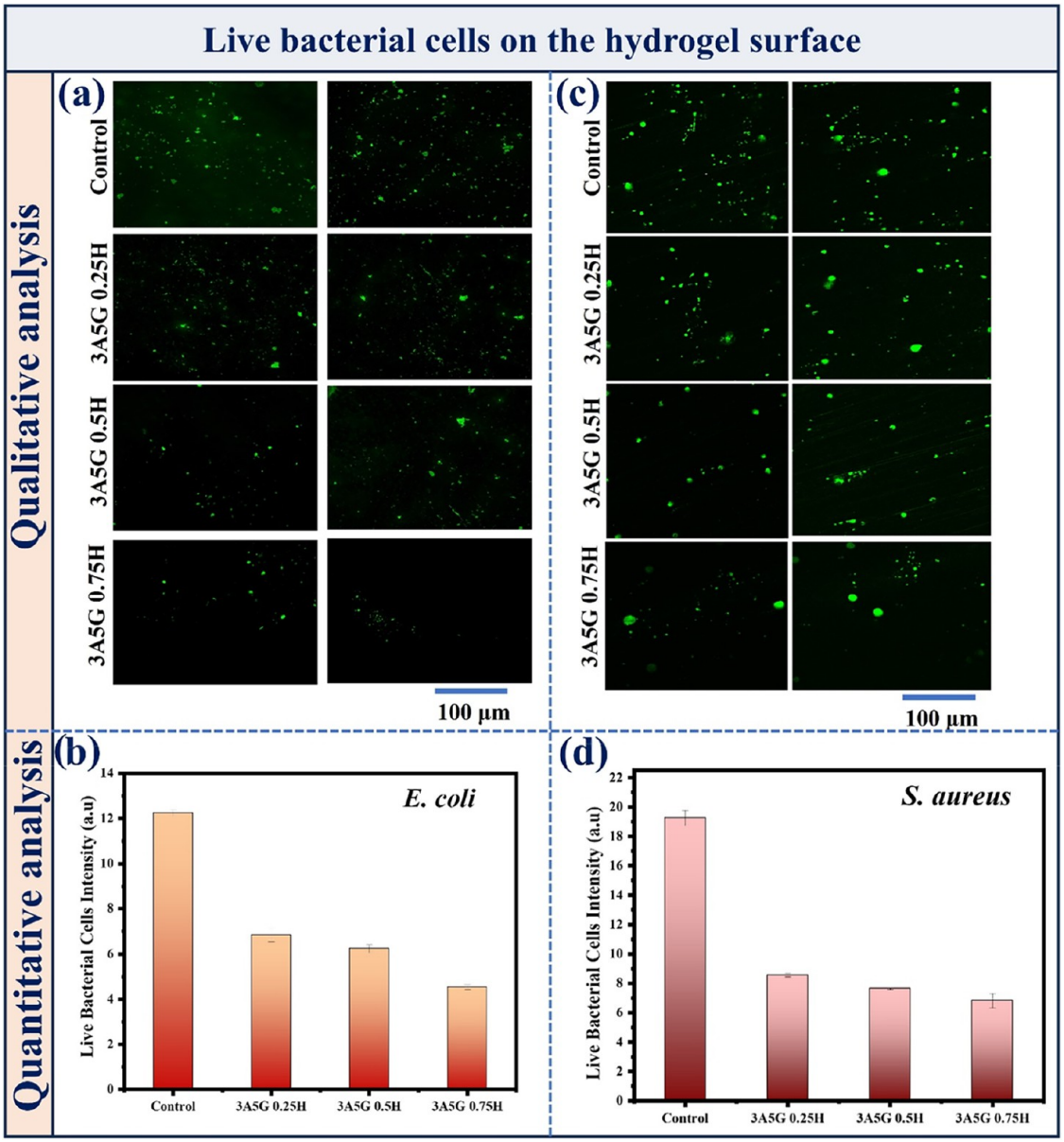

Figure 8. Analysis of the bacterial cell viability on the cross-linked nanohydroxyapatite-reinforced alginate−gelatin hydrogel surface (3A5G0.25H, 3A5G0.5H, and 3A5G0.75H) through the staining of live bacteria by confocal microscopy. (a, b) Qualitative and quantitative evaluation with respect to live *E. coli* bacteria on the cross-linked hydrogel surface. (c, d) Qualitative and quantitative evaluation with respect to live *S. aureus* bacteria on the cross-linked hydrogel surface.

analysis was performed. A range of important parameters such as the pore volume fraction, pore interconnectivity, and pore tortuosity were assessed. The pore volume fraction of the pre-cross-linked hydrogel ink was measured at 62%, while the 3D-printed disc-shaped graft exhibited a pore volume fraction of 74%. For soft tissue reconstruction, scaffolds with a pore volume of 70−90% are ideal for promoting tissue growth.[54,55] This high pore volume ensures adequate space for new tissue formation and allows for effective nutrient and oxygen diffusion as well as efficient waste removal, which is crucial for the development of healthy, integrated tissue [Figure 6].

Pore tortuosity measures the complexity of the pore pathways, indicating how convoluted they are. It is defined as the ratio of the actual path length of the pore to the straight-line distance between two points, as expressed by the following equation.

$$\text{tortuosity} = \text{actual path length}/\text{straight-line distance}$$

In this study, the pore tortuosity values for the pre-cross-linked hydrogel ink and the 3D-printed grafts were 1.13 and 1.09, respectively. A tortuosity value close to 1 suggests relatively straight and uncomplicated pore pathways. This configuration enhances nutrient and oxygen transport, which are crucial for supporting robust tissue growth and promoting effective tissue integration. It ensures optimal conditions for nutrient flow and waste removal within the scaffold [Figure 6].

3.8. Antimicrobial Property. The antimicrobial performance of 3D-printed nanohydroxyapatite (nHAp)-reinforced hydrogel scaffolds (3A5G0.25H, 3A5G0.5H, and 3A5G0.75H) was evaluated against *E. coli* and *S. aureus*, selected as representative Gram-negative and Gram-positive bacteria due to their clinical significance and biofilm-forming ability. CFU analysis demonstrated a progressive reduction in bacterial

https://doi.org/10.1021/acsomega.4c10743
ACS Omega 2025, 10, 18428−18443

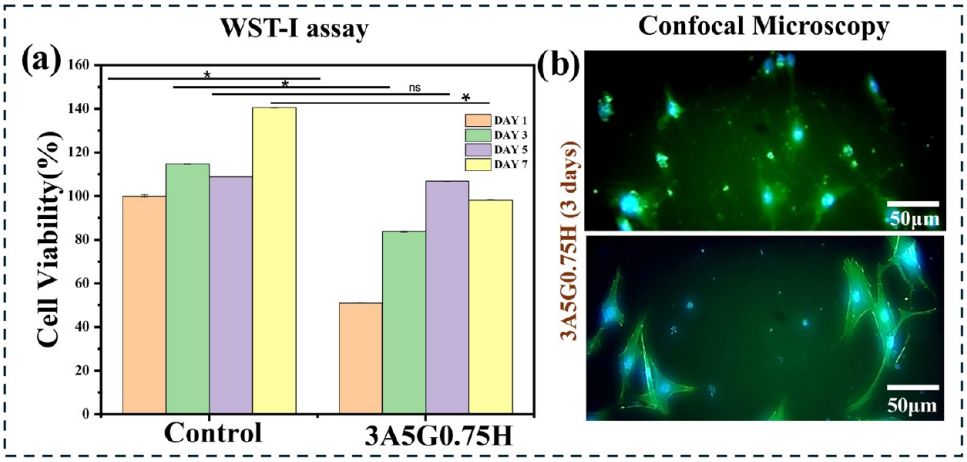

Figure 9. Quantitative and qualitative analyses of cell viability. (a) The outcome of the WST-1 assay to evaluate the percentage of cell viability in the printed scaffolds such as control (3A5G) and 3A5G0.75H. (b) Representative confocal microscopy image of the morphology of the attached cells on the scaffold surface.

colonies with increasing nHAp concentration, as reflected in the log reduction values [Figure 7 and Table 2]. Live/dead imaging further confirmed fewer viable bacteria on hydrogel surfaces with a higher nHAp content compared to the control (3A5G) [Figure 8]. This enhanced antimicrobial efficacy is attributed to the inherent antibacterial properties of nHAp, which facilitate bacterial membrane disruption through Ca^{2+} and PO_4^{3-} ion interactions, as well as the increased matrix stiffness observed in rheological and compressive strength analyses [Figures 3 and 5]. Notably, *E. coli* exhibited greater susceptibility than *S. aureus*, likely due to its thinner peptidoglycan layer and more permeable outer membrane, which allow for increased interaction with nHAp. As a result, higher nHAp concentrations (0.25−0.75%) led to a more pronounced log reduction for *E. coli* than for *S. aureus* [Table 2]. These findings underscore the potential of nHAp-based hydrogels in the development of infection-resistant biomaterial scaffolds.

3.8.1. In Vitro Cytocompatibility. Cell culture studies conducted over various time points, up to 7 days, demonstrated a consistent increase in cell viability for both the control (3A5G) and the 3A5G0.75H scaffolds w.r.to day 1. The selection of the 3A5G0.75H scaffold for in vitro experiments was based on its superior mechanical properties, rheological performance, and antimicrobial efficacy, as previously outlined. Although the high porosity of the 3A5G scaffold posed initial challenges in achieving substantial cell adhesion and viability, a significant improvement in cell viability was observed over time, suggesting that these scaffolds can effectively support cell attachment and proliferation during extended culture periods [Figure 9a].

Furthermore, confocal microscopy was utilized to qualitatively assess the cell morphology on the 3D extrusion-printed scaffold surfaces. Representative confocal images reveal distinct morphological changes, including pronounced filopodial extensions and enhanced cell-to-cell interactions, particularly evident at 3 days of culture [Figure 9b]. These morphological features highlight the favorable cytocompatibility of the scaffolds and confirm their ability to provide a conducive microenvironment for cellular growth and activity during in vitro culture.

4. CONCLUSIONS

Despite advancements in tissue engineering with artificial scaffolds, the reconstruction of complex soft tissues remains limited by persistent challenges with the synthetic hydrogel grafts, primarily due to the inferior strength, stability in physiological conditions, and rejection of the graft primarily by *E. coli*-mediated bacterial infection. In this context, the present study demonstrates the potential efficacy of nanohydroxyapatite addition in terms of tuning the physicochemical properties, such as mechanical strength, rheological behavior, swelling, and degradation behavior of alginate−gelatin-based hydrogel scaffolds. These enhancements in biophysical properties are largely attributed to the strong intermolecular interactions among the primary hydrogel components, alginate and gelatin, and the uniform dispersion of nanohydroxyapatite, which help to maintain gel strength and stability over prolonged periods under physiological conditions. Interestingly, at higher concentrations of nanohydroxyapatite (0.75%), a noticeable increase in compressive strength was observed due to the formation of a reinforced intermolecular network within the hydrogel matrix. The improvement in the stiffness of the hydrogel matrix at a higher concentration of nanohydroxyapatite (0.75%) significantly reduced the bacterial adhesion of *E. coli* and *S. aureus*. The *in vitro* cytocompatibility data demonstrated healthy extended cell morphology and significant improvement in the cell viability of the nanohydroxyapatite-reinforced hydrogel scaffolds.

In summary, the current study critically analyzes the efficacy of nanohydroxyapatite as a potential reinforcing additive in terms of achieving structurally robust 3D-printed tissue-engineered graft along with tailorable biomimetic and also provides an insightful understanding regarding the selection of the best possible nanofillers to modify the hydrogel matrix for tailoring the physicochemical and biophysical properties.

AUTHOR INFORMATION

Corresponding Author

Bikramjit Basu − *Materials Research Centre, Indian Institute of Science, Bangalore 560012, India;* orcid.org/0000-0002-9154-5553; Phone: +91-80-2293 3256; Email: bikram@iisc.ac.in; Fax: +91-80-2360 7316

https://doi.org/10.1021/acsomega.4c10743
ACS Omega 2025, 10, 18428−18443

Authors

Sulob Roy Chowdhury − *Materials Research Centre, Indian Institute of Science, Bangalore 560012, India*

Krittika Dey − *Materials Research Centre, Indian Institute of Science, Bangalore 560012, India*

Complete contact information is available at: https://pubs.acs.org/10.1021/acsomega.4c10743

Notes

The authors declare no competing financial interest.

■ ACKNOWLEDGMENTS

The authors would like to express their sincere gratitude to the Department of Biotechnology (DBT), SERB, the Prime Minister Research Fellowship Scheme, Government of India, the Abdul Kalam Technology Innovation Fellowship, and the NewGen IEDC scheme by DMIMS Wardha for their generous financial support. They also wish to acknowledge the Centre for Nano Science and Engineering (CeNSE), IISc Bangalore, for providing vital characterization facilities, including FT-IR, rheology, microUTM, and dynamic light scattering (DLS) measurements. Additionally, Mr. Sulob extends his appreciation to the Advanced Facility for Microscopy and Microanalysis (AFMM) at IISc Bangalore for granting access to the micro-CT facility.

■ REFERENCES

(1) Langer, R.; Vacanti, J. P. Tissue Engineering. *Science* **1993**, *260*, 920−926.

(2) O'brien, F. J. Biomaterials & scaffolds for tissue engineering. *Mater. Today* **2011**, *14*, 88−95.

(3) Khademhosseini, A.; Langer, R. A decade of progress in tissue engineering. *Nat. Protoc.* **2016**, *11* (10), 1775−1781.

(4) Basu, B. *Biomaterials Science and Tissue Engineering: Principles and Methods*; Cambridge University Press, 2017.

(5) Basu, B. *Biomaterials Science and Implants*, **2020**.

(6) Basu, B.; Ghosh, S. *Biomaterials for Musculoskeletal Regeneration*; Springer: Berlin, Germany, 2017.

(7) Kim, N.; Lee, H.; Han, G.; Kang, M.; Park, S.; Kim, D. E.; Lee, M.; et al. 3D-Printed Functional Hydrogel by DNA-Induced Biomineralization for Accelerated Diabetic Wound Healing. *Adv. Sci.* **2023**, *10* (17), No. 2300816.

(8) Das, S.; Valoor, R.; Ratnayake, P.; Basu, B. Low-Concentration Gelatin Methacryloyl Hydrogel with Tunable 3D Extrusion Printability and Cytocompatibility: Exploring Quantitative Process Science and Biophysical Properties. *ACS Appl. Bio Mater.* **2024**, *7* (5), 2809−2835.

(9) Das, S.; Jegadeesan, T. J.; Basu, B. Advancing peripheral nerve regeneration: 3d bioprinting of GelMA-based cell-laden electroactive bioinks for nerve conduits. *ACS Biomater. Sci. Eng.* **2024**, *10* (3), 1620−1645.

(10) Das, S.; Basu, B. Extrusion-based 3D printing of gelatin methacryloyl with nanocrystalline hydroxyapatite. *Int. J. Appl. Ceram. Technol.* **2022**, *19* (2), 924−938.

(11) Chowdhury, S. R.; Keshavan, N.; Basu, B. Urinary bladder and urethral tissue engineering, and 3D bioprinting approaches for urological reconstruction. *J. Mater. Res.* **2021**, *36* (19), 3781−3820.

(12) Chowdhury, S. R.; Mondal, G.; Ratnayake, P.; Basu, B. Three-Dimensional Extrusion Printed Urinary Specific Grafts: Mechanistic Insights into Buildability and Biophysical Properties. *ACS Biomater. Sci. Eng.* **2024**, *10*, 1040−1061.

(13) Das, S.; Jegadeesan, J. T.; Basu, B. Gelatin Methacryloyl (GelMA)-Based Biomaterial Inks: Process Science for 3D/4D Printing and Current Status. *Biomacromolecules* **2024**, *25* (4), 2156−2221.

(14) Akhtar, M.; Peng, P.; Bernhardt, A.; Gelinsky, M.; Rehman, M. A. U.; Boccaccini, A. R.; Basu, B. Gelatin Methacryloyl (GelMA)-45S5 Bioactive Glass (BG) Composites for Bone Tissue Engineering: 3D Extrusion Printability and Cytocompatibility Assessment Using Human Osteoblasts. *ACS Biomater. Sci. Eng.* **2024**, *10* (8), 5122−5135.

(15) Peppas, N. A.; Hilt, J. Z.; Khademhosseini, A.; Langer, R. Hydrogels in biology and medicine: from molecular principles to bionanotechnology. *Adv. Mater.* **2006**, *18* (11), 1345−1360.

(16) Drury, J. L.; Mooney, D. J. Hydrogels for tissue engineering: scaffold design variables and applications. *Biomaterials* **2003**, *24* (24), 4337−4351.

(17) Hoffman, A. S. Hydrogels for biomedical applications. *Adv. Drug Delivery Rev.* **2012**, *64*, 18−23.

(18) Lee, K. Y.; Mooney, D. J. Hydrogels for tissue engineering. *Chem. Rev.* **2001**, *101* (7), 1869−1880.

(19) Khademhosseini, A.; Langer, R. Microengineered hydrogels for tissue engineering. *Biomaterials* **2007**, *28* (34), 5087−5092.

(20) Tajik, S.; Garcia, C. N.; Gillooley, S.; Tayebi, L. 3D Printing of Hybrid-Hydrogel Materials for Tissue Engineering: A Critical Review. *Regener. Eng. Transl. Med.* **2023**, *9* (1), 29−41.

(21) Jia, J.; Richards, D. J.; Pollard, S.; Tan, Y.; Rodriguez, J.; Visconti, R. P.; Trusk, T. C.; et al. Engineering alginate as bioink for bioprinting. *Acta Biomater.* **2014**, *10* (10), 4323−4331.

(22) Murphy, S. V.; Atala, A. 3D bioprinting of tissues and organs. *Nat. Biotechnol.* **2014**, *32* (8), 773−785.

(23) Blaeser, A.; Campos, D. F. D.; Puster, U.; Richtering, W.; Stevens, M. M.; Fischer, H. Controlling shear stress in 3D bioprinting is a key factor to balance printing resolution and stem cell integrity. *Adv. Healthcare Mater.* **2016**, *5* (3), 326−333.

(24) Gaharwar, A. K.; Peppas, N. A.; Khademhosseini, A. Nanocomposite hydrogels for biomedical applications. *Biotechnol. Bioeng.* **2014**, *111* (3), 441−453.

(25) Gaharwar, A. K.; Avery, R. K.; Assmann, A.; Paul, A.; McKinley, G. H.; Khademhosseini, A.; Olsen, B. D. Shear-thinning nanocomposite hydrogels for the treatment of hemorrhage. *ACS Nano* **2014**, *8* (10), 9833−9842.

(26) Hong, S.; Sycks, D.; Chan, H. F.; Lin, S.; Lopez, G. P.; Guilak, F.; Leong, K. W.; Zhao, X. 3D printing of highly stretchable and tough hydrogels into complex, cellularized structures. *Adv. Mater.* **2015**, *27* (27), No. 4035.

(27) Wilson, S. A.; Cross, L. M.; Peak, C. W.; Gaharwar, A. K. Shear-thinning and thermo-reversible nanoengineered inks for 3D bioprinting. *ACS Appl. Mater. Interfaces* **2017**, *9* (50), 43449−43458.

(28) Roopavath, U. K.; Soni, R.; Mahanta, U.; Deshpande, A. S.; Rath, S. N. 3D printable SiO 2 nanoparticle ink for patient specific bone regeneration. *RSC Adv.* **2019**, *9* (41), 23832−23842.

(29) Markstedt, K.; Mantas, A.; Tournier, I.; Ávila, H. M.; Hagg, D.; Gatenholm, P. 3D bioprinting human chondrocytes with nanocellulose−alginate bioink for cartilage tissue engineering applications. *Biomacromolecules* **2015**, *16* (5), 1489−1496.

(30) Wu, D.; Yu, Y.; Tan, J.; Huang, L.; Luo, B.; Lu, L.; Zhou, C. 3D bioprinting of gellan gum and poly (ethylene glycol) diacrylate based hydrogels to produce human-scale constructs with high-fidelity. *Mater. Des.* **2018**, *160*, 486−495.

(31) Fang, W.; Yang, M.; Wang, L.; Li, W.; Liu, M.; Jin, Y.; Wang, Y.; et al. Hydrogels for 3D bioprinting in tissue engineering and regenerative medicine: Current progress and challenges. *Int. J. Bioprint.* **2023**, *9* (5), No. 759.

(32) Schwab, A.; Levato, R.; D'Este, M.; Piluso, S.; Eglin, D.; Malda, J. Printability and shape fidelity of bioinks in 3D bioprinting. *Chem. Rev.* **2020**, *120* (19), 11028−11055.

(33) Choe, G.; Oh, S.; Seok, J. M.; Park, S. A.; Lee, J. Y. Graphene oxide/alginate composites as novel bioinks for three-dimensional mesenchymal stem cell printing and bone regeneration applications. *Nanoscale* **2019**, *11* (48), 23275−23285.

(34) Wei, Q.; Zhou, J.; An, Y.; Li, M.; Zhang, J.; Yang, S. Modification, 3D printing process and application of sodium alginate

based hydrogels in soft tissue engineering: A review. *Int. J. Biol. Macromol.* **2023**, *232*, No. 123450.
(35) Murab, S.; Gupta, A.; Włodarczyk-Biegun, M. K.; Kumar, A.; van Rijn, P.; Whitlock, P.; Han, S. S.; Agrawal, G. Alginate based hydrogel inks for 3D bioprinting of engineered orthopedic tissues. *Carbohydr. Polym.* **2022**, *296*, No. 119964.
(36) Saravanou, S. F.; Ioannidis, K.; Dimopoulos, A.; Paxinou, A.; Kounelaki, F.; Varsami, S. M.; Tsitsilianis, C.; Papantoniou, I.; Pasparakis, G. Dually crosslinked injectable alginate-based graft copolymer thermoresponsive hydrogels as 3D printing bioinks for cell spheroid growth and release. *Carbohydr. Polym.* **2023**, *312*, No. 120790.
(37) Liu, C.; Qin, W.; Wang, Y.; Ma, J.; Liu, J.; Wu, S.; Zhao, H. 3D printed gelatin/sodium alginate hydrogel scaffolds doped with nano-attapulgite for bone tissue repair. *Int. J. Nanomed.* **2021**, *16*, 8417−8432.
(38) Chen, Q.; Tian, X.; Fan, J.; Tong, H.; Ao, Q.; Wang, X. An interpenetrating alginate/gelatin network for three-dimensional (3D) cell cultures and organ bioprinting. *Molecules* **2020**, *25* (3), No. 756.
(39) Geevarghese, R.; Somasekharan, L. T.; Bhatt, A.; Kasoju, N.; Nair, R. P. Development and evaluation of a multicomponent bioink consisting of alginate, gelatin, diethylaminoethyl cellulose and collagen peptide for 3D bioprinting of tissue construct for drug screening application. *Int. J. Biol. Macromol.* **2022**, *207*, 278−288.
(40) Chen, X.; Sun, L.; Wang, H.; Cao, S.; Shang, T.; Yan, H.; Lin, Q. Nano-SiO2 reinforced alginate-chitosan-gelatin nanocomposite hydrogels with improved physicochemical properties and biological activity. *Colloids Surf., B* **2023**, *228*, No. 113413.
(41) Kim, Y. B.; Lee, H.; Kim, G. H. Strategy to achieve highly porous/biocompatible macroscale cell blocks, using a collagen/genipin-bioink and an optimal 3D printing process. *ACS Appl. Mater. Interfaces* **2016**, *8*, 32230−32240.
(42) Quinlan, E.; López-Noriega, A.; Thompson, E.; Kelly, H. M.; Cryan, S. A.; O'Brien, F. J. Development of collagen−hydroxyapatite scaffolds incorporating PLGA and alginate microparticles for the controlled delivery of rhBMP-2 for bone tissue engineering. *J. Controlled Release* **2015**, *198*, 71−79.
(43) Zhu, K.; Shin, S. R.; van Kempen, T.; Li, Y.-C.; Ponraj, V.; Nasajpour, A.; Mandla, S.; et al. Gold nanocomposite bioink for printing 3D cardiac constructs. *Adv. Funct. Mater.* **2017**, *27* (12), No. 1605352.
(44) Van Vlierberghe, S.; Dubruel, P.; Schacht, E. Biopolymer-based hydrogels as scaffolds for tissue engineering applications: a review. *Biomacromolecules* **2011**, *12* (5), 1387−1408.
(45) Yang, G.; Xiao, Z.; Long, H.; Ma, K.; Zhang, J.; Ren, X.; Zhang, J. Assessment of the characteristics and biocompatibility of gelatin sponge scaffolds prepared by various crosslinking methods. *Sci. Rep.* **2018**, *8* (1), No. 1616.
(46) Negrini, N. C.; Tarsini, P.; Tanzi, M. C.; Farè, S. Chemically crosslinked gelatin hydrogels as scaffolding materials for adipose tissue engineering. *J. Appl. Polym. Sci.* **2019**, *136* (8), No. 47104.
(47) Mondal, A.; Gebeyehu, A.; Miranda, M.; Bahadur, D.; Patel, N.; Ramakrishnan, S.; Rishi, A. K.; Singh, M. Characterization and printability of Sodium alginate-Gelatin hydrogel for bioprinting NSCLC co-culture. *Sci. Rep.* **2019**, *9* (1), No. 19914.
(48) Ghorbani, F.; Kim, M.; Monavari, M.; Ghalandari, B.; Boccaccini, A. R. Mussel-inspired polydopamine decorated alginate dialdehyde-gelatin 3D printed scaffolds for bone tissue engineering application. *Front. Bioeng. Biotechnol.* **2022**, *10*, No. 940070.
(49) Urruela-Barrios, R.; Ramírez-Cedillo, E.; de León, A. D.; Alvarez, A. J.; Ortega-Lara, W. Alginate/gelatin hydrogels reinforced with TiO2 and β-TCP fabricated by microextrusion-based printing for tissue regeneration. *Polymers* **2019**, *11* (3), No. 457.
(50) Damiri, F.; Fatimi, A.; Musuc, A. M.; Santos, A. C. P.; Paszkiewicz, S.; Idumah, C. I.; Singh, S.; Varma, R. S.; Berrada, M. Nano-hydroxyapatite (nHAp) scaffolds for bone regeneration: Preparation, characterization and biological applications. *J. Drug Delivery Sci. Technol.* **2024**, *95*, No. 105601.
(51) Kumar, B. Y. S.; Isloor, A. M.; Kumar, G. C. M.; Inamuddin; Asiri, A. M. Nanohydroxyapatite reinforced chitosan composite hydrogel with tunable mechanical and biological properties for cartilage regeneration. *Sci. Rep* **2019**, *9*, No. 15957.
(52) Nabavinia, M.; Khoshfetrat, A. B.; Naderi-Meshkin, H. Nano-hydroxyapatite-alginate-gelatin microcapsule as a potential osteogenic building block for modular bone tissue engineering. *Mater. Sci. Eng., C* **2019**, *97*, 67−77.
(53) Ma, P.; Wu, W.; Wei, Y.; Ren, L.; Lin, S.; Wu, J. Biomimetic gelatin/chitosan/polyvinyl alcohol/nano-hydroxyapatite scaffolds for bone tissue engineering. *Mater. Des.* **2021**, *207*, No. 109865.
(54) Zeng, Z.; Song, P.; Gui, X.; Zhang, B.; Zhao, L.; Feng, P.; Deng, Z.; et al. 3D printed Nanohydroxyapatite/Polyamide 66 scaffolds with balanced mechanical property and osteogenic ability for bone repair. *Mater. Des.* **2024**, *241*, No. 112896.
(55) Ribeiro, M.; de Moraes, M. A.; Beppu, M. M.; Garcia, M. P.; Fernandes, M. H.; Monteiro, F. J.; Ferraz, M. P. Development of silk fibroin/nanohydroxyapatite composite hydrogels for bone tissue engineering. *Eur. Polym. J.* **2015**, *67*, 66−77.

https://doi.org/10.1021/acsomega.4c10743
ACS Omega 2025, 10, 18428−18443